RESEARCH ARTICLE

Nonintrusive measurements of mixture concentration fields by analyzing diffraction image patterns (point spread function) of nanoparticles

Jae-Sung Park · Kenneth D. Kihm · Joon Sik Lee

Abstract The diffraction image patterns of small particles are referred to as their point spread function (PSF); these patterns vary distinctively with the refractive index (RI) of a transparent test medium when the particles are imaged through the medium. The RI correlates directly with the mixture concentration, so proper inversion of measured PSFs can provide full-field information on the mixture concentration field. In this study, fluorescent nanoparticles of 500 nm diameter are fixed on a glass surface by means of evaporative self-assembly, and the time-varying test mixture is placed in front of the glass surface. The time-varying and full-field PSF distributions are imaged and digitally analyzed to determine the local RI values as well as the local mixture concentrations. Both immiscible water/oil mixture and miscible water/glycerol mixture are imaged. The present method shows an RI measurement to have an uncertainty of $\pm 5 \times 10^{-3}$ RIU and the mixture concentration measurements to have uncertainty of approximately 4%.

J.-S. Park · K. D. Kihm (✉)
Mechanical, Aerospace, and Biomedical Engineering,
University of Tennessee, Knoxville,
TN 37996-2210, USA
e-mail: kkihm@utk.edu

J. S. Lee
School of Mechanical and Aerospace Engineering,
Seoul National University, Seoul 151-742,
Republic of Korea

Present Address:
J.-S. Park
BK21 School for Creative Engineering Design of Next
Generation Mechanical and Aerospace Systems,
Seoul National University, Seoul, Republic of Korea

1 Introduction

When an infinitesimally small point source is imaged through microscopic optics, the resulting three-dimensional diffraction image pattern (Fig. 1) is called point spread function (PSF), which modulates both longitudinally and laterally (Born and Wolf 1999). Good analytical descriptions of PSF are given in classical archives (Cagnet et al. 1962; Richards and Wolf 1959); in addition, Gibson and Lanni (1991) presented a practical equation for PSF that accounts for optical aberrations caused by non-designed specimen structures. PSF also approximates the diffraction patterns of small but finite particles such as the nanoparticles under consideration.

Diffraction generally degrades optical images; this is truer for highly magnified micro/nano-scale imaging. Many studies, therefore, concentrated on identifying the diffraction image degradation and suggesting improvements to minimize the degradation effect. For example, studies on microscale particle image velocimetry (PIV) have struggled with the diffraction problem of fluorescent tracer particles (Meinhart et al. 1999; Raffel et al. 2007; Santiago et al. 1998). Researchers have performed analytical investigations into diffraction images in PIV in terms of volume illumination and the out-of-focus effect of the microscopy system (Meinhart et al. 2000; Meinhart and Wereley 2003; Olsen and Adrian 2000). In other studies, an instrumental innovation associated with confocal laser scanning microscopy (CLSM) was shown to be certainly less subject to the off-focused and noisy images caused by optical diffraction compared to the conventional wide-field microscopy (Park et al. 2004; Pawley and Masters 2008).
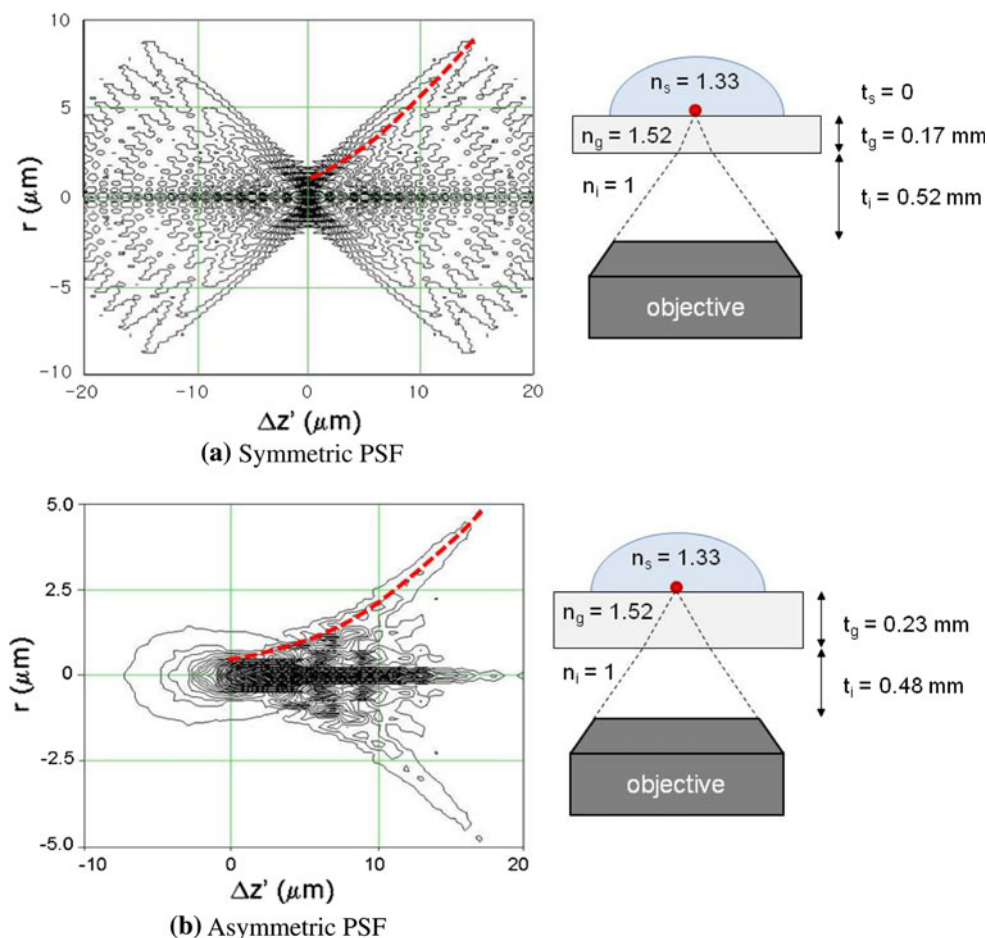
Approaching the problem from a different direction, Agard (1984) used optical serial sectioning microscopy (OSSM) to get depth-wise image resolution out of optically

(a) Symmetric PSF

(b) Asymmetric PSF

diffracted and degraded images. The principle is that the level of diffraction/degradation depends on the depth-wise locations as demonstrated in Fig. 1. Subsequently, a series of studies have been done using the diffraction for depth-wise particle tracking tasks such as defocusing digital PIV (Pereira and Gharib 2002), 3-D tracking of nanoparticle locations (Speidel et al. 2003), 3-D particle tracking velocimetry (Wu et al. 2005; Luo et al. 2006), deconvolution microscopy for microfluidics (Park and Kihm 2006), and the development of thermometry based on Brownian motion detection of suspended nanoparticles (Hohreiter et al. 2002; Park et al. 2005).

In the present paper, a novel approach for detecting mixture concentrations is proposed based on the correlation of the test fluid RI with corresponding nanoparticle diffraction image patterns. RI of fluidic mixture varies linearly with mixture concentrations in most cases, and proper inversion of PSF provides the fluidic RI as well as the fluidic mixture concentration fields. Nanoparticles are prepared by being spatially fixed by means of evaporative self-assembly on a glass surface behind the fluid, and their diffraction patters reflect the optical path length changes because of the fluidic RI changes. Digital analysis of their

diffraction patterns allows full-field detection of time-dependent mixture concentrations with a microscale spatial resolution.

2 Theoretical background

The analytical expression of PSF assumes an integral form that consists of the Bessel function and a sinusoidal complex exponential term (Gibson and Lanni 1991). The resulting 3-D light intensity distribution is given in terms of the radial location (r_d) and the defocus distance (Δz) as:

$$I(r_d, \Delta z) = \left| C \int_0^1 J_o \left[k \frac{NA}{\sqrt{M^2 - NA^2}} r_d \rho \right] \exp[jW(\Delta z, \rho)] \rho d\rho \right|^2$$

(1)

Here, $r_d = \sqrt{x_d^2 + y_d^2}$, k is the wave number, which is equivalent to $2\pi/\lambda$ with λ being the emission wavelength of the point source, NA is the numerical aperture of the objective lens, M is the total magnification of the microscopic imaging system, and ρ is the normalized radius in the exit pupil plane.

The phase aberration function, $W(\Delta z, \rho)$, is the product of the wave number (k) and the optical path difference (OPD) that is calculated with the following equation.

$$
\begin{aligned}
\mathrm{OPD} \approx\; & n_{\mathrm{i}} \Delta z \sqrt{1-\left(\frac{\mathrm{NA}\rho}{n_{\mathrm{i}}}\right)^2} + n_{\mathrm{s}} t_{\mathrm{s}} \left\{ \sqrt{1-\left(\frac{\mathrm{NA}\rho}{n_{\mathrm{s}}}\right)^2} \right. \\
& \left. - \frac{n_{\mathrm{i}}^2}{n_{\mathrm{s}}^2}\sqrt{1-\left(\frac{\mathrm{NA}\rho}{n_{\mathrm{i}}}\right)^2} \right\} \\
& + n_{\mathrm{g}} t_{\mathrm{g}} \left\{ \sqrt{1-\left(\frac{\mathrm{NA}\rho}{n_{\mathrm{g}}}\right)^2} - \frac{n_{\mathrm{i}}^2}{n_{\mathrm{g}}^2}\sqrt{\left(\frac{\mathrm{NA}\rho}{n_{\mathrm{i}}}\right)^2} \right\} \\
& - n_{\mathrm{g}*} t_{\mathrm{g}*} \left\{ \sqrt{1-\left(\frac{\mathrm{NA}\rho}{n_{\mathrm{g}*}}\right)^2} - \frac{n_{\mathrm{i}}^2}{n_{\mathrm{g}*}^2}\sqrt{1-\left(\frac{\mathrm{NA}\rho}{n_{\mathrm{i}}}\right)^2} \right\} \\
& - n_{\mathrm{i}*} t_{\mathrm{i}*} \left\{ \sqrt{1-\left(\frac{\mathrm{NA}\rho}{n_{\mathrm{i}*}}\right)^2} - \frac{n_{\mathrm{i}}^2}{n_{\mathrm{i}*}^2}\sqrt{1-\left(\frac{\mathrm{NA}\rho}{n_{\mathrm{i}}}\right)^2} \right\}
\end{aligned}
\tag{2}
$$

where n and t are the refractive index and the thickness of each optical layer. The subscripts s, g, i indicate the respective layers of specimen fluid, cover glass, and immersion medium as shown in Fig. 1. The symbol * means the design conditions of these parameters. In this multi-layer configuration of object, the defocus distance (Δz) is defined as

$$
\frac{\Delta z}{n_{\mathrm{i}}} = \frac{t_{\mathrm{s}}}{n_{\mathrm{s}}} + \frac{t_{\mathrm{g}}}{n_{\mathrm{g}}} + \frac{t_{\mathrm{i}}}{n_{\mathrm{i}}} - \frac{t_{\mathrm{g}*}}{n_{\mathrm{g}*}} - \frac{t_{\mathrm{i}*}}{n_{\mathrm{i}*}}
\tag{3}
$$

The OPD is the difference between two optical paths (weighted by the local RI) connecting an identical point source and imaging end point in both design and non-design systems. A more detail about the derivation of OPD is available from Gibson and Lanni (1991). They mentioned that the OPD was determined with a few assumptions that the front surface of the first lens element is planar and the lens is designed to obey the sine condition between the design object and image planes ensuring a zero-coma image. Also, they found that sufficiently closed parallel rays, entering a high-NA spherical lens system, travel equal optical paths and pass at the same point in the back-focal plane. Finally, the OPD can be determined with the difference in optical paths traveled by the two rays from the object points of design and non-design systems to the points at which they enter the lens system as parallel rays (Gibson and Lanni 1991).

Aberration-free imaging is achieved only when the microscope system is tuned to the design conditions (OPD = 0) required for the test specimen, cover glass material and thickness, immersion medium, and objective lens specifications. The design condition stipulates that the light ray from the point source travels through a cover glass of designated refractive index and thickness and an immersion medium of designated refractive index and thickness. Also, the specimen thickness must be zero to ensure aberration-free imaging. The corresponding "symmetric" PSF is shown in Fig. 1a.

Almost all practical cases in the laboratory, however, are subject to image aberration, since the thickness and refractive index of specimen cannot be zero. Moreover, when the cover glass used is different from the specified one, the phase aberration becomes more substantial, and the resulting 3-D PSF will be further distorted and not symmetric as shown in Fig. 1b. The aberrant diffraction pattern normally consists of a stack of concentric fringes; and its outermost fringe usually holds the highest intensity, as marked in red. When all optical and material conditions are identical, the ring patterns at a fixed imaging plane change only with RI of the test fluid. The idea is to correlate the outermost fringe diameter (D_{omf}) with the local RI of the fluidic mixture, so that we can determine the local mixture concentrations. Indeed, it was difficult to derive numerically the correlation between D_{omf} and RI from the diffraction model of Eq. (1). A number of outmost fringe diameters were gained by plotting PSF in terms of RI and thickness of different media, and then the correlation curves could be determined by a data curve fitting.

3 Experiment

3.1 Microscopic imaging system

Our method uses an asymmetric PSF generated by a non-designed specimen. The specimen, consisting of cover glasses and test fluid, was placed between the spatially fixed fluorescent nanoparticles in the background and an objective lens in the foreground (Fig. 2). We use an epi-fluorescent system based on an inverted microscope (IX 70, Olympus Inc.) equipped with a high-NA objective lens (Universal Plan Semi-Apochromat $60\times$; water immersion; NA 1.1; Olympus Inc.), a beam-splitting mirror unit (U-MNB2, Olympus Inc.), and a mercury lamp for the fluorescence illuminator (U-LH 100HG, Olympus Inc.). The beam-splitting mirror unit consisted of a band pass excitation filter with a central wavelength of 480 nm and a bandwidth of 20 nm, a dichroic mirror with an interfacial wavelength of 500 nm, and a long pass emission filter with an interfacial wavelength of 520 nm.

A charge-coupled device (CCD) camera with a $1{,}000 \times 1{,}000$ array of square 8-μm pixels with 14-bit resolution (C9100-02, Hamamatsu Inc.) was mounted on the video port of microscope to record digital images of the diffraction patterns that were transmitted to a computer via a commercial frame grabber board (Hamamatsu Inc.). A specimen was placed on a two-axis mechanical stage, so
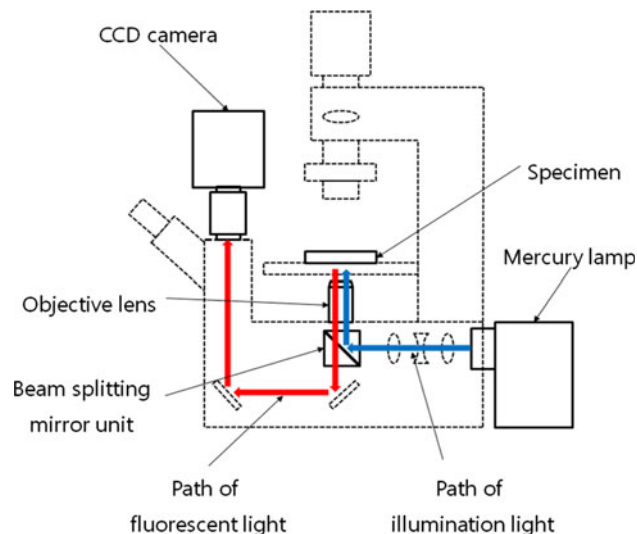
Fig. 2 The experimental setup uses an epi-fluorescent system based on an inverted microscope (IX 70, Olympus Inc.) equipped with a high-NA objective lens (60× 1.1 NA), a beam-splitting mirror unit, and a mercury lamp for fluorescence illuminator. The illumination light is filtered at 480 nm, and the fluorescent emission is centered at 520 nm. A Hamamatsu 14-bit CCD with 1,000 × 1,000 pixel resolution records diffraction patterns of nanoparticles that are spatially fixed on the outer surface of the specimen

that the lateral positioning of the image focus could be achieved. The objective lens was moved to get axial positioning of the image focus.

3.2 Fabrication of specimen

The specimen was fabricated using two cover glasses of 150 µm thickness with 1.515 RI for the top and bottom of the microchannel and with a uniform gap of about 92 µm (Fig. 3). Fluorescently labeled 500-nm polystyrene microspheres (#F8813, Invitrogen Corp.) were selected as point sources of diffraction, and they self-assembled by evaporation onto the top cover glass. The cover glasses were treated with a plasma generator, and the nanoparticle suspension was containing a small amount of surfactant (Tween 20). Due to the physicochemical treatments, particles were dispersed homogeneously with a minimal aggregation on the hydrophilic glass surface.

The source (fluorescent bead) of the point spread function should be as small as possible yet not undergo photobleaching or diminishing signal intensity because of the small source sizes. On the image plane of the present infinity-corrected optical system, the diffraction-limited spot size of fluorescent particles is estimated to 35 µm using $d_s = 1.22(M + 1)\lambda/\text{NA}$ (Meinhart and Wereley 2003). The corresponding diffraction-limited spot size on the object plane is then estimated to 580 nm. Thus, source particles that are smaller than 500 nm would substantially
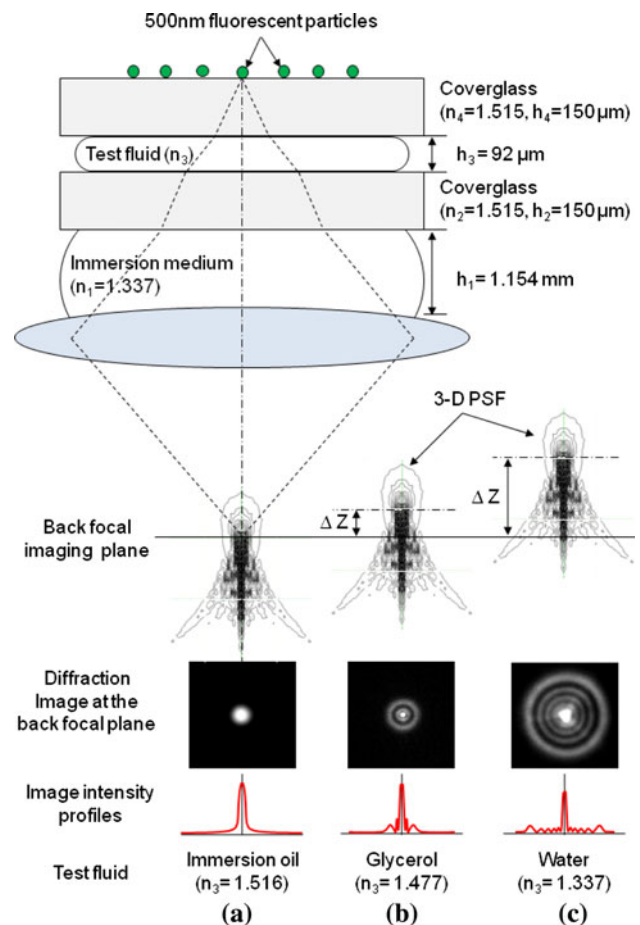

Fig. 3 Schematic layout of test specimen and illustration of formation of diffraction fringe images for fluids with different refractive index values. Three-dimensional PSF patterns and their meridian projections on the reference focal plane are presented for three different test fluids: **a** immersion oil ($n = 1.516$), **b** glycerol ($n = 1.477$), and **c** water ($n = 1.337$) for the specified test configuration. The lower refractive index values of glycerol and water alter the defocusing level (Δz) from the reference focal imaging plane set for immersion oil

weaken the intensity of fringe patterns. The use of 500 nm is believed to play a proper role as a point source of PSF as well as to sustain an acceptably high signal to noise ratio in the fringe measurement.

The microspheres had excitation/emission wavelength maxima at 505/515 nm, respectively, and worked efficiently with the beam-splitting mirror unit and the mercury lamp. The fluorescence emission spectrum of microsphere used in this study has a narrow bandwidth of about $\Delta\lambda = 40$ nm (Molecular Probes 2005). Thus, the emitted fluorescence light should be a quasi-monochromatic wave lines. The coherence length of this light source can be estimated by the definition of $L_c = \lambda^2/\Delta\lambda$, where λ is an average emission wavelength. The estimated coherence length is about 6.63 µm ($\sim 13\lambda$). The objective distance, h_1, which was filled with the immersion medium (water),

was set at 1.154 mm for the preliminary testing and in the case of the two immiscible fluids, composed of water and oil (Sect. 4.1), and at 1.167 mm in the case of the miscible fluids, which were composed of water and glycerol (Sect. 4.2).

3.3 Detection of the outermost fringe diameter (D_{omf})

The first row of the inset Fig. 3a–c shows the meridian projection of PSFs for immersion oil ($n = 1.516$), glycerol ($n = 1.477$), and water ($n = 1.337$), respectively, using Eq. (1); the second row shows their corresponding diffraction patterns measured at the back-focal imaging plane. The third row of images presents the cross-sectional intensity profiles at the back-focal plane. The absolute frame of reference in recording D_{omf} is focused on the plane close to the diffraction limited spot size of nanoparticle in this optical system (Fig. 3a). The defocusing distance, Δz, presents the amplitude of PSF along the optical axis. The Δz increases with increasing deviations of RI from the arbitrarily selected reference of the immersion oil ($\Delta z = 0$), and the outermost fringe diameter, D_{omf}, at the back-focal plane also increases with the deviation. Note that the phase of design condition PSF is changed by the optical aberration of the non-design condition (Δz, n, and t), as shown in Fig. 1. In addition, the change in RI of specimen results in the phase and amplitude changes in non-design PSF.

Figure 4 shows a decreasing correlation of the outermost fringe diameter (D_{omf}) with an increasing RI of the test fluid. Comparison of the measured D_{omf} with the numerically calculated D_{omf}, based on Eq. (1), shows fairly good agreement. The extended bars represent the rms
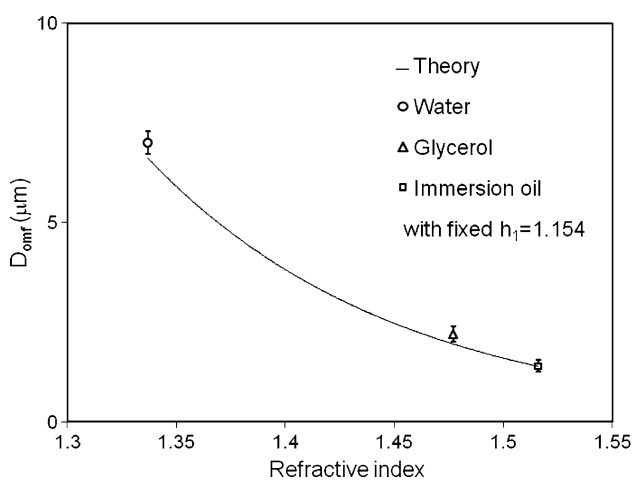

Fig. 4 Comparison of measured out-most-fringe diameter (D_{omf}) with theory of Eq. (1) for water ($n = 1.337$), glycerol ($n = 1.477$), and immersion oil ($n = 1.516$) using the same configuration shown in Fig. 3. The error bars represent the rms variations of ten different realizations for D_{omf} measurements

variation of the measured diameters for ten (10) realizations. The theory predicts the peak location of the outermost fringe by identifying the radial location where the most drastic slope change takes place in the total integrated power function of intensity, which is defined as

$$e(r_d, \triangle z) = \int_0^{r_0} \int_0^{2\pi} I(r_d, \triangle z) r dr d\phi. \tag{4}$$

4 Results and discussion

Section 4.1 presents an example of a stationary and distinct interface between two immiscible fluids of water and oil, and Sect. 4.2 presents the moving, smeared interface between two miscible fluids of water and glycerol. Section 4.3 presents discussions on the overall uncertainty for the mixture concentration measurements.

4.1 Immiscible water/oil interface

The first experiment used immersion oil ($n = 1.516$ at 22°C) and water ($n = 1.337$ at 22°C) to examine the nanoparticle image patterns near the discrete interface between the two immiscible fluids. Figure 5 shows the optical diffraction patterns of fluorescent nanoparticles in the region near the stationary interface between oil and water. The diffraction patterns go through a distinct transition from the oil region to the water region. Different optical path lengths spanning different fluid regions create different diffraction patterns. Propagations of spherical waves emitted from the spatially fixed fluorescent particles are schematically illustrated, followed by the corresponding diffraction patterns.

The experimental parameters and conditions were tuned to generate well-focused images of the fluorescent particles, such like in Fig. 3a, for the 100% oil region that is far from the interface (Fig. 5a). For the location near the interface (Fig. 5b), portion of the spherical wave penetrates the water region and experiences a different optical path length. The resulting image is a hybrid of the focused image, representing the oil region, and the partially constructed fringes, representing the water region. At the precise location of the interface (Fig. 5c), the fringes occupy one-half of the images, showing that the "fan" angle of fringes can be a good indication for the relative measurement location with respect to the interface location. This finding is confirmed for the location passing from the interface into the water region (Fig. 5d), where more than half of the spherical waves pass the water region, and the fringes dominate the image, leaving small, defective fringes on the left, indicating the interfering effect of the oil

Fig. 5 Diffraction image patterns of spatially fixed fluorescent nanoparticles in the vicinity of the stationary interface between immiscible water and immersion oil. The propagation of spherical waves emitted from nanoparticles schematically illustrates their distortions from circular fringes when passing both fluids to conform to diffraction images. Therefore, the resulting fringes show distinctively different patterns depending on the relative locations of nanoparticles to the interface: **a** oil region more than 150 μm away from the interface, **b** oil side approximately 80 μm from the interface, **c** right at the interface, **d** water side about 80 μm from the interface, and **e** water region more than 150 μm away from the interface
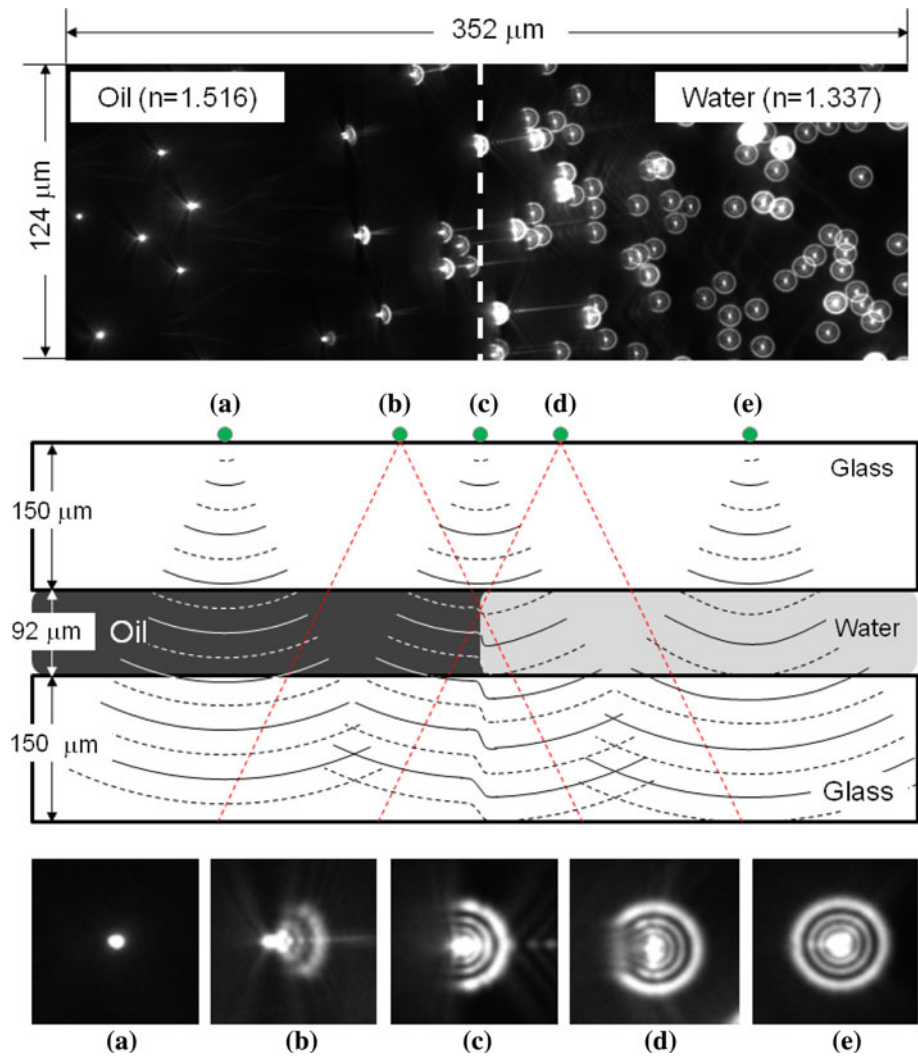
region. For the pure water region away from the interface (Fig. 5e), fully circular diffraction images were recovered, as seen in Fig. 3c.

The outermost fringe diameter D_{omf} was measured at 6.5 μm for water (Fig. 5e) and 1.3 μm for oil (Fig. 5a), and these data agree well with both theoretical predictions and the previous measurement data shown in Fig. 4. In the vicinity of the interface, the spherical waves created from a single source of a fluorescent nanoparticle were seen to have split into two regions experiencing different optical path lengths. The resulting hybridized fringes can be used as an indication of the relative measurement locations from the interface and can also be used to identify the precise location of the interface where the fan angle of the fringe image approaches 180°.

As shown in Fig. 5, the width of non-physical region around the interface showing fan-shape fringe patterns is an order of 100 μm depending upon separation situation. Unfortunately, it is a very difficult problem to examine, in detail, the local refractive index near the interfacial region

because of the unknown slope of the interface. The interface may be shaped either in linearly tilted or non-linearly curved. Note that we presumed the vertical interface in the immiscible case of Fig. 5. The width of this atypical region can tell clues on the spatial resolution of the technique measuring the interface between immiscible fluids. From the geometrical consideration, we expect the measurement spatial resolution to be also related to the slope of interface and partially to the numerical aperture and the microchannel thickness as well.

4.2 Miscible water/glycerol interface

The second experiment used two miscible fluids of glycerol and water to create a mixing region with continuously varying mixture concentrations. The corresponding refractive index of the mixture varied from 1.477 for 100% glycerol to 1.337 for 100% water, both at 22°C. A small amount of water was dropped on a microchannel inlet to be absorbed by means of capillarity and to fill a microchannel

of a cross-section 92 μm high and 2 mm wide, and shortly after, a few drops of glycerol was dropped at the same inlet, so that it could come into direct contact with water and penetrate with it into the channel (Fig. 6). Within a short period time, a diffusive mixing region formed between the two fluids. The diffusive flow of glycerol into water was driven by a pressure difference between inlet and outlet after a good volume of glycerol was dropped on the inlet. The water was drained out of the outlet by the pressure driven flow, and the percentage of glycerol in the microchannel was gradually increased up to 100%. In order to amplify the fringe sizes for more distinctive pattern recognition, the objective distance, h_1, was intentionally biased to 1.167 mm from the design condition of 1.154 mm (Fig. 3).

The temporally expanded schematic at the top of Fig. 7 illustrates the progressive penetration of glycerol into water inside a microchannel, showing the continual increase in the glycerol concentration at the interface in time. Figure 7a shows consecutive images of outermost fringe diameter changing (D_{omf}) from 17.6 μm for 100% water at $t = 0s$ to 8.3 μm for 100% glycerol at $t = 5s$. The solid curve in Fig. 7b represents the theoretical correlation of D_{omf} with the mixture refractive index values. The symbols present the measured D_{omf}, and the error bars indicate rms variations of the measurements. Assuming a linear variation of refractive index in proportion to the mixture concentration (Mettler Toledo 2007), the glycerol concentration can be determined from the mixture refractive index, and thus, ultimately from the measured D_{omf}, as shown in Fig. 7b.

This new measurement technique allows us to nonintrusively determine the mixture concentration distributions by analyzing the optical fringes formed in the mixing region based on the 3-D PSF of nanoparticles. A number of previous researchers studied microfluidic mixing by visually tracking seeded fluorescent particles in one of the two mixing fluids (Strook et al. 2002, and many others

thereafter). Fluidic mixing, however, is a progressive molecular diffusion, and the tracking of suspended nanoparticles does not ensure the actual representation of the molecular phenomena. What makes the present technique unique is that the nanoparticles as a point source of diffraction are spatially fixed and located outside the fluid region, so that the mixture may be completely label free, and the true molecular diffusion can be observed without being interrupted by foreign particles.

4.3 Measurement uncertainties

In this experiment, we consider two measurement uncertainties, i.e., the difference between theoretical and measured values of D_{omf} and the accuracy of refractive index estimation of test fluid. The measurement uncertainty originally starts from the resolution of diffraction image in a microscopy system. The measurement value of D_{omf} had a tolerance of 0.133 μm, which was determined by the 8-μm pixel size of the CCD chip and the 60× magnification of the microscope. In Fig. 4, the fringe diameters were determined from the average of 10 different diffraction fringes, and the rms errors were about ±2 pixels corresponding to a physical dimension of ±0.267 μm. On the other hand, the increased error bars up to 0.9 μm shown in Fig. 7 are attributed to the enhanced measurement uncertainties because of the slightly oval fringe patterns.

Parametric uncertainties such as layer thicknesses and refractive index values can also contribute to the overall uncertainties. This can results in additional discrepancies between the predictions and measurements in both Figs. 4 and 7. The discrepancies are estimated to range from 0.1 to 0.3 μm in the fringe diameter. Noting that refractive index is measured from D_{omf}, the measurement uncertainty of the refractive index determination is estimated to be approximately ±0.005 in RIU as a conservative estimation. This corresponds to ±4% uncertainty in determining glycerol concentrations in the mixture with water.

Fig. 6 A schematic illustration of the mixing configuration of two miscible fluids (water and glycerol) in a microchannel. The glycerol flow is continually introduced into the originally water filled microchannel until the entire channel is substituted by 100% glycerol
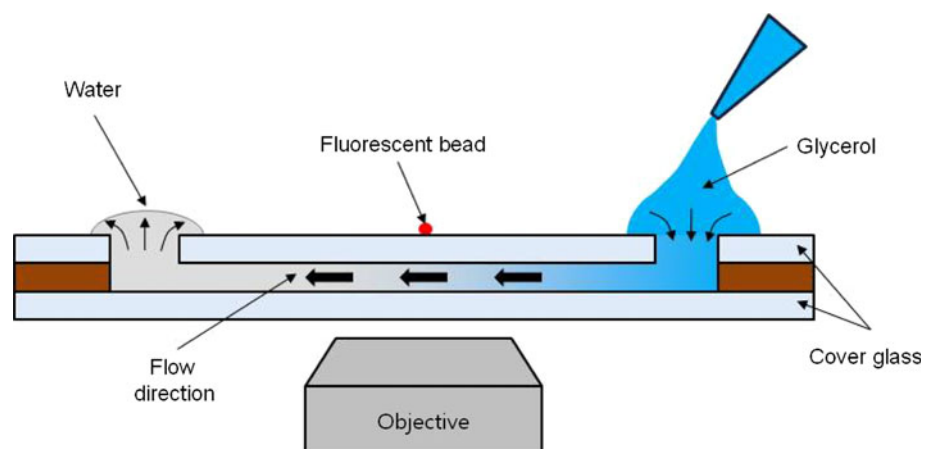
Fig. 7 For the case of glycerol penetrating into water inside a microchannel, **a** the glycerol concentration in the interfacial region increases with time, showing persistent decrease of out-most-fringe diameter D_{omf}, and **b** the measured D_{omf} and the refractive index change from 17.6 μm and 1.337 (100% water at $t = 0$) to 8.3 μm and 1.477 (100% glycerol at $t = 5s$). The *solid curve* in *b* shows the theoretical predictions for D_{omf} for the objective distance $h_1 = 1.167$ mm, filled with immersion medium
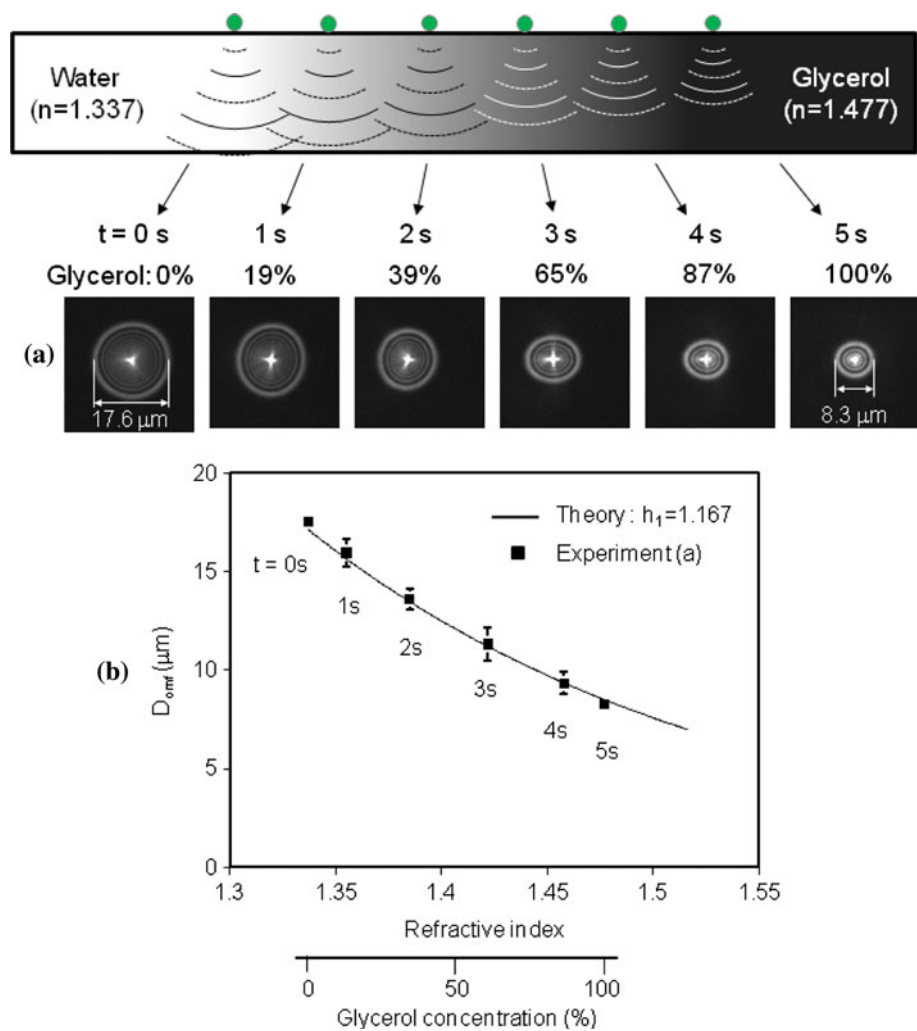
5 Conclusion

A novel technique using defocused diffraction images of fluorescent nanoparticles (3-D PSF) has been successfully developed to determine the refractive index values and volumetric concentrations of fluid mixtures. The fluorescent nanoparticles are placed outside the channel wall, so that the tested fluids can be label free while the diffraction images of the spatially fixed nanoparticles carry information on different optical path length through the fluid at different locations with different mixture concentrations. Furthermore, by examining the shape and completeness of the diffraction fringes, the proposed technique is able to determine the precise location of the interface between two immiscible fluids (water + oil) and to identify the broadened mixing region for the case of two miscible fluids (water + glycerol).

References

Agard DA (1984) Optical sectioning microscopy: cellular architecture in three dimensions. Ann Rev Biophys Bioeng 13:191–219

Born M, Wolf E (1999) Principles of optics, 7th edn. Cambridge University Press, New York

Cagnet M, Francon M, Thrierr JC (1962) Atlas of optical phenomena. Springer-Verlag, Berlin

Gibson FS, Lanni F (1991) Experimental test of an analytical model of aberration in an oil-immersion objective lens used in three-dimensional light microscopy. J Opt Soc Am A 8:1601–1613

Hohreiter V, Wereley ST, Olsen MG, Chung JN (2002) Cross-correlation analysis for temperature measurement. Meas Sci Technol 13:1072–1078

Luo R, Sun YF, Peng XF, Yang XY (2006) Tracking sub-micron fluorescent particles in three dimensions with a microscope objective under non-design optical conditions. Meas Sci Technol 17:1358–1366

Meinhart CD, Wereley ST (2003) The theory of diffraction-limited resolution in microparticle image velocimetry. Meas Sci Technol 14:1047–1053

Meinhart CD, Wereley ST, Santiago JG (1999) PIV measurements of a microchannel flow. Exp Fluids 27(5):414–419

Meinhart CD, Wereley ST, Gray MHB (2000) Volume illumination for two-dimensional particle image velocimetry. Meas Sci Technol 11:809–814

Mettler T (2007) Refractive index concentration tables. In the following website address: http://us.mt.com/mt/filters/applications_analytical_refractometry/Refractometry_concentration_tables_browse_0x000248e100025ba40005d14e.jsp

Molecular Probes (2005) Fluospheres fluorescent microspheres. In the following website address: http://probes.invitrogen.com/media/pis/mp05000.pdf

Olsen MG, Adrian RJ (2000) Out-of-focus effects on particle image visibility and correlation in microscopic particle image velocimetry. Exp Fluids Suppl:166–174

Park JS, Kihm KD (2006) Three-dimensional micro-PTV using deconvolution microscopy. Exp Fluids 40(3):491–499

Park JS, Choi CK, Kihm KD (2004) Optically sliced micro-PIV using confocal laser scanning microscopy (CLSM). Exp Fluids 37(1):105–119

Park JS, Choi CK, Kihm KD (2005) Temperature measurement for nanoparticle (500-nm) suspension by detecting the Brownian motion using optical serial sectioning microscopy (OSSM). Meas Sci Technol 16:1418–1429

Pawley JB, Masters BR (2008) Handbook of biological confocal microscopy, third edition. J Biomed Opt 13(2):029902

Pereira F, Gharib M (2002) Defocusing digital particle image velocimetry and the three-dimensional characterization of two-phase flows. Meas Sci Technol 13:683–694

Raffel M, Willert CE, Wereley ST, Kompenhans J (2007) Particle image velocimetry, 2nd edn. Springer, Berlin, pp 241–258

Richards B, Wolf E (1959) Electromagnetic diffraction in optical systems II. Structure of the image field in an aplanatic system. Proc R Soc A 253:358–379

Santiago JG, Wereley ST, Meinhart CD, Beebe DJ, Adrian RJ (1998) A particle image velocimetry system for microfluidics. Exp Fluids 25(4):316–319

Speidel M, Jonas A, Florin EL (2003) Three-dimensional tracking of fluorescent nanoparticles with subnanometer precision by use of off-focus imaging. Opt Lett 28:69–71

Strook AD, Dertinger SKW, Ajdari A, Mezic I, Stone HA, Whitesides GM (2002) Chaotic mixer for microchannels. Science 295:647–651

Wu M, Roberts JW, Buckley M (2005) Three-dimensional fluorescent particle tracking at micron-scale using a single camera. Exp Fluids 38:461–465